coatings

MDPI

*Article*

# Flexible Finely and Directly Patternable Liquid Metal Electrodes via Selective Surface Wetting Technique

**Seong Ju Park and Chanwoo Yang ***

Advanced Nano-Surface & Wearable Electronics Research Laboratory, Heat and Surface Technology R&D Department, Korea Institute of Industrial Technology, Incheon 21999, Republic of Korea
* Correspondence: chanu@kitech.re.kr

**Abstract:** Eutectic gallium–indium (EGaIn) is an ideal material for preparing flexible electrodes, but its high surface tension poses a challenge during deposition and patterning. Herein, we propose a laser-induced selective surface wetting technique (SSWT) to enable the facile and straightforward fabrication of flexible finely and directly patternable EGaIn liquid metal electrodes. Our proposed technique selectively controls the wettability of EGaIn by establishing a perfluorinated self-assembled monolayer on a zinc oxide nanorod array to impart superhydrophobicity and then inducing specific sites on the hydrophilized surface by ultraviolet (UV) pulsed laser ablation, thereby enabling fine patterning (linewidth, ~50 μm). Surface analysis of the effect of laser ablation was also performed to elucidate the mechanism of SSWT. The patterned EGaIn liquid metal electrode fabricated by SSWT exhibited superior flexibility, with a resistance change ($\Delta R/R_0$) of only 18.6% compared with a Ag thin film electrode, which showed a dramatic increase in $\Delta R/R_0$ to nearly 500% after 50,000 folding cycles at a peak strain of 2.5%. The simple and easily implementable liquid metal patterning technique proposed in this study may potentially be applied in the field of wearable and stretchable electronics, which requires extreme flexibility.

**Keywords:** liquid metals; eutectic indium gallium; pulsed laser ablation; patterning; ZnO nanorods; self-assembled monolayer; flexible electrodes; cyclic bending fatigue

check for updates

**Citation:** Park, S.J.; Yang, C. Flexible Finely and Directly Patternable Liquid Metal Electrodes via Selective Surface Wetting Technique. *Coatings* **2023**, *13*, 1922. https://doi.org/10.3390/coatings13111922

Academic Editors: Aomar Hadjadj, Shibing Liu, Haiying Song and Xuewu Li

Received: 28 September 2023
Revised: 3 November 2023
Accepted: 8 November 2023
Published: 10 November 2023

**Copyright:** © 2023 by the authors. Licensee MDPI, Basel, Switzerland. This article is an open access article distributed under the terms and conditions of the Creative Commons Attribution (CC BY) license (https://creativecommons.org/licenses/by/4.0/).

## 1. Introduction

Flexible electronics is an expanding research area that focuses on the creation of electronic devices capable of being bent, twisted, or stretched without impeding their functionality [1]. These unique capabilities enable new form factors, such as carrying in a folded or rolled state or attachment to the body. Recently, the field of flexible electronics has advanced to the point of mimicking human skin with bio-inspired robotic skin for sliding tactile perception [2]. Maintaining device performance under stress from deformation is a critical aspect of flexible device design. All device components must possess flexibility and the ability to distribute the stress caused by deformation to ensure device durability after mechanical deformation. The application of brittle materials to flexible device components can result in damage and breakdown owing to stress during deformation [3]. Liquid metals offer an attractive alternative to rigid materials for flexible electrodes. These metals can remain in a liquid state at room temperature because their melting points are below or near room temperature. This state provides liquid metals with unique advantages over other metals, such as the ability to flow, bend, and reform at room temperature [4]. However, their use is limited to specific applications owing to the inherent radioactivity of cesium, the high instability of francium and rubidium, and the toxicity of mercury [5].

Fortunately, unlike other liquid metals, eutectic gallium–indium (EGaIn) alloy does not have such limitations. The conductivity of EGaIn ($\sigma = 3.4 \times 10^6$ S m$^{-1}$) is comparable with that of other metals [6]. Thus, EGaIn not only exhibits high electrical conductivity but also withstands folding and stretching stress, rendering it ideal for use as a flexible electrode

material on account of its outstanding features. Chen et al. reported self-healing, robustly conductive, and stretchable conductors by embedding EGaIn liquid-metal patterns within an imprintable self-healing elastomer [7]. EGaIn is an ideal material for flexible electrodes, but its high surface tension poses a challenge during deposition and patterning. Several methods, such as direct inkjet printing, photolithography, injection molding, and stamp lithography, have been proposed to control the patterning of EGaIn liquid metals [8–13]. However, these methods have limitations when applied to actual production owing to factors such as time consumption, low resolution, and complexity. Jiang et al. reported the direct patterning of EGaIn liquid metal by inducing selective wettability differences via a laser ablation process; however, the authors did not perform a surface analysis of the effects of the laser ablation process and did not show the realization of fine linewidths below 50 μm [14].

Herein, we present a cost-effective, easily customizable, and direct patterning approach for liquid EGaIn via a selective surface wetting technique (SSWT). A superhydrophobic surface was created by establishing a fluorine-containing self-assembled monolayer (SAM) on a zinc oxide (ZnO) nanorod array using a straightforward hydrothermal synthesis method under atmospheric conditions. Because the ZnO nanorods react favorably to ultraviolet (UV) light, a UV pulsed laser can selectively hydrophilize the surface. Thereafter, EGaIn was brushed onto and effectively coated on the selectively hydrophilized surface. We demonstrate that EGaIn liquid metal can form micropatterns with fine linewidths of as low as 50 μm. Furthermore, the EGaIn liquid metal patterned electrode displayed superb flexibility after 50,000 cycles of folding fatigue.

## 2. Materials and Methods

### 2.1. Materials

A 1-mm-thick soda–lime glass slide (Paul Marienfeld, 1000412, Berlin, Germany) and a 50-μm-thick polyethersulfone film (PES, SU30-FM-000150, GoodFellow, Huntingdon, UK) were used as substrates. Zinc acetate dihydrate (99.999%, Sigma-Aldrich, St. Louis, MO, USA) and 1-propanol (99.5%, Sigma-Aldrich) were used as the solute and solvent, respectively, for the ZnO seed coating solution. Zinc nitrate hexahydrate (98%, Sigma-Aldrich) and hexamethylenetetramine (99.5%, Sigma-Aldrich) were used for ZnO growth. For superhydrophobic surface treatment, 1H,1H,2H,2H-perfluorooctyltriethoxysilane (PFOTES, 98%, Sigma-Aldrich), butylamine (99.5%, Sigma-Aldrich), and toluene were used as the self-assembling molecules, catalyst, and SAM solution solvent, respectively. Diiodomethane (DIM, 99%, Sigma-Aldrich) was used to calculate the surface energy ($\gamma_s$) from the droplet contact angles of the hydrophilized surfaces. EGaIn electrodes were purchased from MIDAS (Seoul, Korea) and used as conductive electrodes (Ga:In = 75.5:24.5 wt%).

### 2.2. Fabrication of Patterned EGaIn Electrodes

A schematic diagram of the fabrication process of the patterned EGaIn electrode is shown in Figure 1. The process for fabricating a selectively wettable substrate includes seed-layer coating (Figure 1b), ZnO-nanorod growth (Figure 1c), superhydrophobic treatment with the PFOTES SAM (Figure 1d), UV pulsed laser ablation (Figure 1e), and EGaIn brush deposition (Figure 1f). The substrates were cleaned by sonication with isopropyl alcohol, acetone, and deionized (DI) water and treated with UV ozone for 10 min. A 10 mM solution of zinc acetate dihydrate (99.999%, Sigma-Aldrich) in 1-propanol was spin-coated on the cleaned substrates at 2000 rpm for 30 s. The samples were then baked at 130 °C for 1 min. The above coating and baking process was repeated five times to ensure the uniform coverage of the zinc acetate crystallites on the substrate. All samples were pre-annealed in an air atmosphere at 200 °C for 1 h to obtain ZnO seeds. For ZnO nanorod growth, the samples were soaked in 25 mM zinc nitrate hexahydrate and 25 mM hexamethylenetetramine in DI water and heated in a microwave oven (2.45 GHz) at 1000 W for 3 min. The residual solvent in the samples was removed by rinsing with DI water [15]. Next, the samples were immersed in 1 mM PFOTES and a solution of 0.01 vol% butylamine

in toluene at 45 °C for 90 min to form a SAM composed of PFOTES molecules on the ZnO nanorods. The treated samples were rinsed with toluene to remove excess PFOTES molecules [16]. The superhydrophobic samples were selectively ablated by a nanosecond UV pulsed laser (LSU5DS 3D Laser Marking System, HGTECH, Wuhan, China), as shown in Figure 1e, to expose the hydrophilic surfaces of channels with different widths. The widths of the laser-ablated channels were 50, 100, 200, 500, and 1000 μm. The wavelength of the laser was 355 nm, the pulse frequency was 100,000 Hz, the off time was 6500 ns, and the scan rate was 1000 mm/s. Finally, EGaIn liquid metal patterns were formed on the selectively wettable substrate using a brush, as shown in Figure 1f.

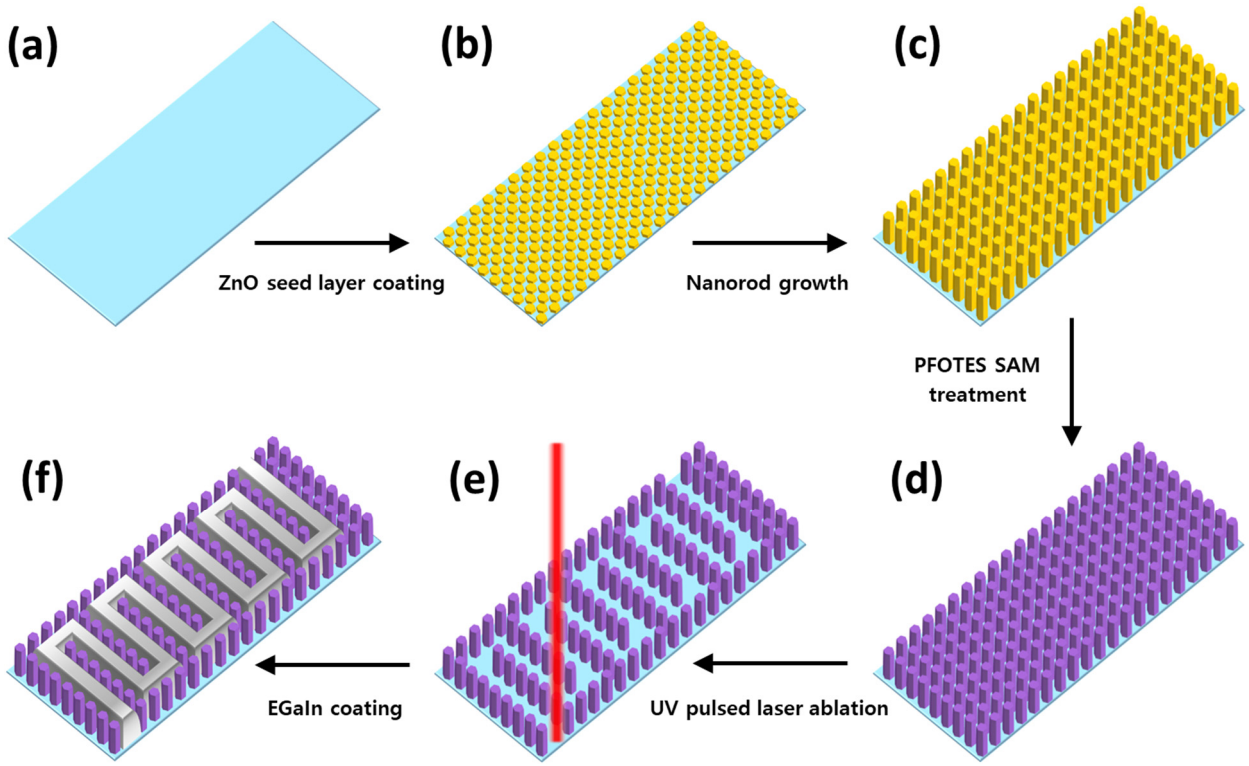


**Figure 1.** Schematic of the fabrication process of patterned EGaIn electrodes via SSWT: (**a**) substrate cleaning, (**b**) ZnO seed layer coating on the substrate and pre-annealing, (**c**) ZnO nanorod growth fabricated by microwave heating, (**d**) PFOTES SAM treatment on the ZnO nanorods, (**e**) UV pulsed laser ablation, (**f**) EGaIn patterns on the selectively wettable substrate using a brush.

### *2.3. Characterization*

The surface top-view and cross-section of the samples were characterized using a field emission scanning electron microscope (FE-SEM, NOVA-600, FEI, Hillsboro, OR, USA) equipped with an energy-dispersive X-ray spectrometer (EDS). X-ray diffraction (XRD, X'Pert-Pro MPD, Malvern Panalytical, Malvern, UK) analysis was performed to investigate the crystal structure of the ZnO nanorods. The absorbance of the samples was analyzed using a UV-Vis spectrophotometer (UV-2550, Shimadzu, Kyoto, Japan) to characterize their optical absorption at 355 nm. A drop shape analyzer (DSA100, KRÜSS, Hamburg, Germany) was used to measure the contact angles of DI water and DIM droplets on the hydrophilized samples. Here, 3 μL of the liquids was applied to the surface of each sample. Images of the obtained EGaIn conductive patterns and the ablation linewidths were captured by optical microscopy (OM, BX51M, OLYMPUS, Tokyo, Japan). Folding tests were performed for 50,000 cycles using CFT-070i equipment (COVOTECH, Hwaseong-si, Korea) to demonstrate the flexibility of the EGaIn conductive layer, and electrical resistances were measured and averaged every 10,000 cycles using a two-point probe multimeter (Fluke 289, Fluke, Everett, WA, USA). The resistance change ($\Delta R/R_0$) was calculated as $\Delta R/R_0 = (R - R_0)/R_0$, where $R$ is the resistance after folding and $R_0$ is the initial resistance.

## 3. Results and Discussion

Figure 2 shows top-view images of the laser-ablated interface region of the PFOTES SAM-processed ZnO nanorod array layer (hereafter referred to as ZnO-PFOTES) at different magnifications. The ZnO nanorods were grown on the substrate and then subjected to selective laser irradiation to enable the analysis of the laser-irradiated and pristine surfaces using FE-SEM and EDS. The ZnO nanorods grew uniformly and densely, as shown in Figure 2a. The surface images of the non-irradiated area on the left and the laser-irradiated area on the right were compared, as demonstrated in Figure 2b. The noticeable difference in morphology between these areas subjected to laser irradiation and those without it was apparent. Redeposited ZnO nanorod fragments from laser ablation were detected. One-dimensional EDS analysis (distance, ~2220 μm) was performed on the boundary region to investigate whether the ZnO nanorods were well-ablated by the UV pulsed laser, as shown in Figure 2c,d. The laser-ablated region exhibited a significantly lower Zn-Kα intensity than the non-ablated area, which was consistent with the results obtained from the FE-SEM top-view image shown in Figure 2b. Hence, based on the FE-SEM and EDS analysis, the use of the UV pulsed laser was confirmed to lead to the removal of the ZnO-PFOTES layer.

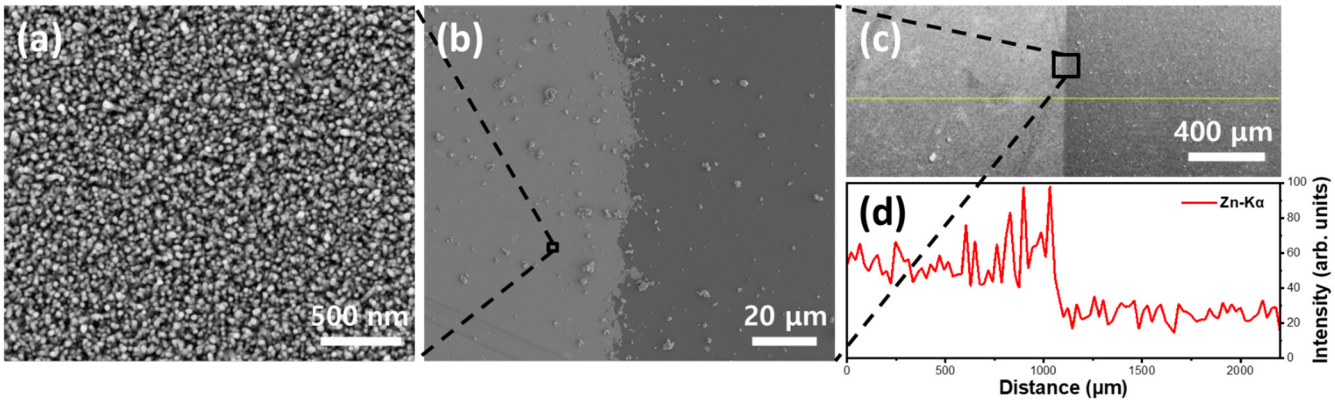


**Figure 2.** FE-SEM top-view images of (**a**) pristine ZnO-PFOTES and (**b**,**c**) laser-ablated interface area. (**d**) EDS line scan Zn-Kα spectrum of the laser-ablated interface area (yellow line in (**c**)).

The crystallinity and optical characteristics of the pristine and laser-ablated ZnO-PFOTES were investigated by XRD and UV-Vis, respectively, to further confirm successful ablation by the UV pulsed laser, as shown in Figure 3. In the case of the pristine ZnO-PFOTES, ZnO crystal growth was more dominant along the z-axis than along the x-axis, which was confirmed by the stronger intensity of the (002) plane at 34.4° than that of the (100) plane at 31.8°, as shown in Figure 3a. This result aligns well with the FE-SEM image in Figure 2c and previous studies on hydrothermally synthesized ZnO nanorods, which showed a dominant tendency for z-axis growth [17]. The presence of ZnO was also confirmed by the absorbance peak at 369 nm, which is an inherent absorption characteristic of ZnO, as shown in Figure 3b [18]. In contrast, the XRD peaks and absorption peak of ZnO at 369 nm were considerably diminished in the laser-ablated ZnO-PFOTES. ZnO-PFOTES exhibited a broad absorption peak at 355 nm and a central wavelength of 369 nm, as shown in Figure 3b. Thus, ZnO-PFOTES was effectively eliminated by the UV-pulsed laser with a central wavelength of 355 nm.

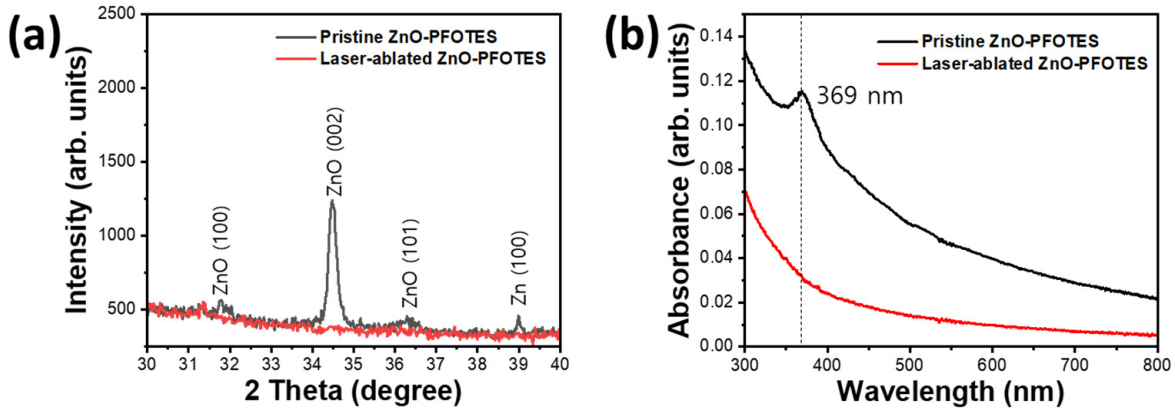


**Figure 3.** (**a**) Out-of-plane XRD patterns and (**b**) UV-Vis optical absorption spectra of the pristine (black line) and laser-ablated (red line) ZnO-PFOTES samples.

The general mechanism of laser ablation involves the absorption of light energy, where excited electrons transfer heat to the lattice due to photon absorption, causing the heating effect to melt or vaporize the material, resulting in macroscopic removal of material from the substrate [19]. This phenomenon occurs when the peak fluence ($F_0$) of the laser is above the ablation threshold fluence ($F_{th}$) and is calculated as follows [20]:

$$D^2 = 2w^2 \ln\left(\frac{F_0}{F_{th}}\right), \quad (1)$$

where $D$ and $w$ are the ablation linewidth and $1/e^2$ beam radius of the Gaussian beam profile, respectively. The peak fluence of the Gaussian laser beam is calculated from the pulse energy ($E$) of the UV pulsed laser with the following equation:

$$F_0 = \frac{2E}{\pi w^2} \quad (2)$$

Figure 4 shows the correlation of the ablation linewidth with the peak fluence of the UV pulse laser. Figure 4a shows the OM images of the laser scanning ablation trace lines of the ZnO-PFOTES layer at different laser pulse energies. The higher the pulse energy of the laser, the more the ablation linewidth of the ZnO-PFOTES layer tended to increase. This phenomenon is a natural consequence of the Gaussian profile of the laser beam, which increases the portion of the laser beam with higher fluence as the pulse energy increases [20]. In general, the higher the irradiation fluence, the higher the absorbed energy density, which induces higher temperatures. As a result, a larger portion of the irradiated area is ablated, and the ablation linewidth increases (Figure 4b). From these results, the calculated ablation threshold fluence for the ZnO-PFOTES was 5.01 J/cm$^2$ from the x-intercept obtained by extrapolation from Equation (1) and Figure 4c.

The Droplet contact angle analysis was adopted to quantitatively calculate the change in $\gamma_s$ induced by laser ablation. Table 1 shows the $\gamma_s$ characteristics and droplet shapes of liquids on the pristine and laser-ablated ZnO-PFOTES.

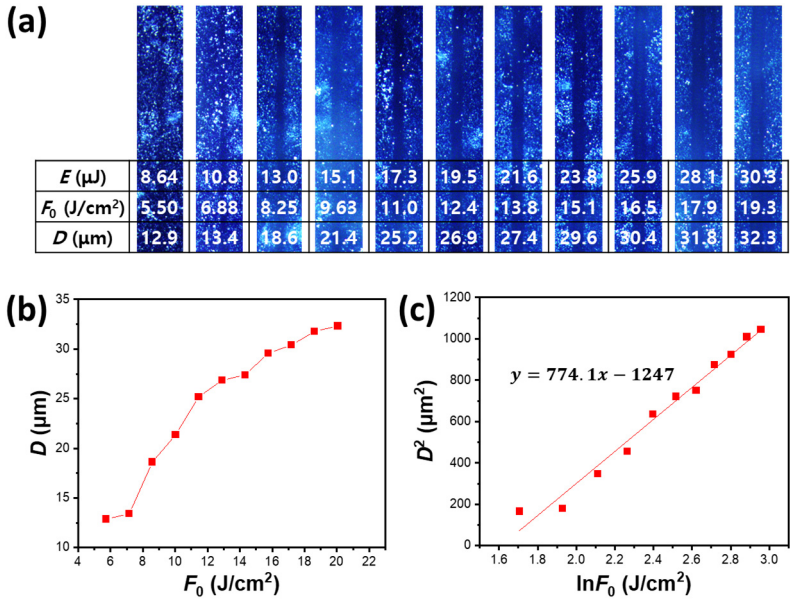


**Figure 4.** (**a**) OM images and ablation linewidths of laser scanning ablation trace lines of the ZnO-PFOTES layer as a function of peak fluence calculated with different laser pulse energies, (**b**) ablation linewidth as a function of laser peak fluence, and (**c**) plot of the square of the ablation linewidth versus the natural logarithm of peak fluence.

**Table 1.** Surface energy ($\gamma_s$) characteristics and droplet shapes of liquids on the pristine and laser-ablated ZnO-PFOTES samples.

| Sample | Contact Angle (°) | | $\gamma_s^p$ (mJ m$^{-2}$) | $\gamma_s^d$ (mJ m$^{-2}$) | $\gamma_s$ (mJ m$^{-2}$) | $X_p\left(=\gamma_s^p/\gamma_s\right)$ |
|---|---|---|---|---|---|---|
| | DI Water | DIM | | | | |
| Pristine ZnO-PFOTES | 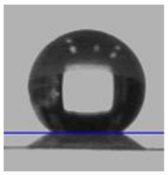 141.0 | 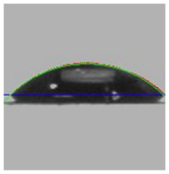 70.63 | 5.906 | 29.01 | 34.92 | 0.1691 |
| Laser-ablated ZnO-PFOTES | 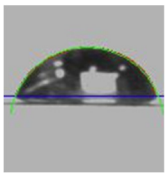 42.87 | 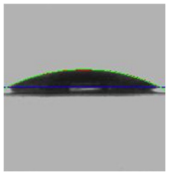 26.50 | 24.71 | 33.97 | 58.68 | 0.4210 |

The contact angles of the DI water and DIM droplets on pristine ZnO-PFOTES were 141° and 70.63°, respectively, while those on the laser-ablated ZnO-PFOTES were 42.87° and 26.5°, respectively. The DI water contact angle of 141° on the pristine ZnO-PFOTES sample is much larger than 90°, which means the sample exhibits superhydrophobicity owing to the lotus effect induced by the nanostructure of ZnO-PFOTES [21]. Surface energy $\gamma_s$, which is an indicator of the strength of intermolecular forces in a sample and is related to its wettability, can be calculated using the following equations [22,23]:

$$1+\cos\theta=\frac{2\left(\gamma_s^d\right)^{1/2}\left(\gamma_{lv}^d\right)^{1/2}}{\gamma_{lv}}+\frac{2\left(\gamma_s^p\right)^{1/2}\left(\gamma_{lv}^p\right)^{1/2}}{\gamma_{lv}}, \quad (3)$$

$$\gamma_s = \gamma_s^p + \gamma_s^d, \tag{4}$$

$$X_p = \frac{\gamma_s^p}{\gamma_s}, \tag{5}$$

where $\gamma_s^p$ and $\gamma_s^d$ refer to the surface energies of the polar and dispersive components of the sample, respectively, and $\gamma_{lv}$ is the surface tension of the test liquid. The quantitative $\gamma_s$ values of the samples were obtained by inserting the known values of $\gamma_{lv}$, $\gamma_{lv}^d$, and $\gamma_{lv}^p$ of the test liquids [22] and the measured contact angle $\theta$ into the above equation. The $\gamma_s$, $\gamma_s^d$, and $\gamma_s^p$ calculated for the pristine ZnO-PFOTES were 34.92, 29.01, and 5.906 mJ/m$^2$, respectively, while those calculated for the laser-ablated ZnO-PFOTES were 58.68, 33.97, and 24.71 mJ/m$^2$, respectively. Because $\gamma_s$ increased from 34.92 to 58.68 mJ/m$^2$ and the polar component ratio $X_p$ increased from 0.1691 to 0.4210 following laser ablation, the selective wetting of EGaIn was clearly facilitated by this process.

Figure 5 displays the different EGaIn patterns created using SSWT. In Figure 5a, the line patterns of EGaIn formed on the PES substrate had varying linewidths of 50, 100, 200, 500, and 1000 μm. Electrical resistance was successfully measured in all patterned EGaIn lines. The resistance increased considerably as the linewidth decreased. However, even at the narrowest linewidth of 50 μm, an accurate measurement of resistance was still obtained, indicating a seamless patterning process. Magnified OM images of the 50, 100, and 200 μm fine-line patterns are shown in Figure 5b–d, respectively. The advantage of laser for designing patterns is demonstrated in Figure 5e, which shows the text pattern formed using SSWT as a digitalized process. Although some dewetting areas are evident in the enlarged OM images shown in Figure 5f,g, the overall patterns demonstrated good resolution with clear boundary definitions.

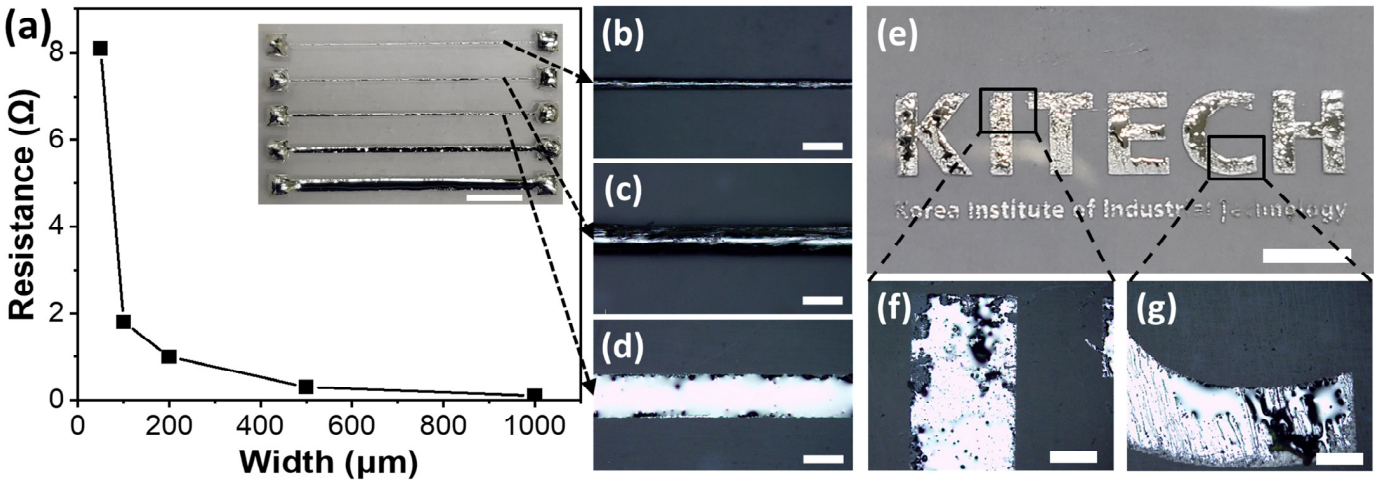


**Figure 5.** (**a**) Electrical resistance and OM image (inset) of flexible EGaIn electrodes with different patterned linewidths of 50, 100, 200, 500, and 1000 μm. Scale bar = 5 mm. (**b**–**d**) OM images of the fine-line patterns with linewidths of 50, 100, and 200 μm, respectively. Scale bar = 200 μm. (**e**) Text logo pattern and (**f**,**g**) enlarged OM images of the areas marked in (**e**). Scale bars = (**e**) 5 mm and (**f**,**g**) 500 μm.

Figure 6 shows the inward-folding cyclic fatigue-deformation characteristics of patterned EGaIn liquid metal and Ag thin film electrodes. The stability of the electrodes under cyclic folding was estimated by assessing $\Delta R/R_0$. The EGaIn and Ag electrodes on the flexible PES film substrate were fabricated by SSWT and sputtering, respectively. When

electrodes on a film substrate are folded at 180°, the peak strain ($\varepsilon$) on the sample surface could be determined using the following equation:

$$\varepsilon = \frac{t}{2r}, \tag{6}$$

where $t$ is the thickness of the substrate and $r$ is the bending radius [24,25]. In the cyclic folding test, $t$ and $r$ were 50 µm and 1 mm, respectively, corresponding to a peak strain of 2.5%. The cyclic folding test was performed in five sets of 10,000 cycles to achieve a total of 50,000 cycles, and resistance measurements were taken every 10,000 cycles. The $\Delta R/R_0$ the Ag electrode increased dramatically to over 150% after 10,000 cycles and increased linearly to almost 500% after 50,000 cycles. Most electrodes composed of thin film metals, including those made of Ag, have been reported to fracture at strains below 2% when used on polymer substrates [24,25]. Therefore, in this study, the cyclic folding test was performed at a peak strain of 2.5%, which is greater than the fracture strain, resulting in a sharp change in resistance. In contrast, the $\Delta R/R_0$ of the EGaIn electrode increased moderately to ~15% and then remained stable over subsequent measurements, increasing to only 18.6% after 50,000 cycles. This result is attributed to EGaIn's higher flexibility resulting from its much lower Young's modulus ($2.1 \times 10^5$ Pa) compared to Ag metal ($\sim 5 \times 10^9$ Pa) [26–28]. Thus, compared with the Ag thin film electrode, the EGaIn liquid metal electrode fabricated with SSWT was much more stable against cyclic folding fatigue owing to the flexibility of the intrinsic liquid state of EGaIn. To compare with previously reported findings on flexible electrodes, we defined an $\varepsilon N$ value (in this work, $\varepsilon N$ = 2.5% × 50,000 = 1250) to represent the degree of cyclic folding fatigue, where $N$ is the number of folding cycles, as shown in Figure 6b. Most previous studies on flexible electrodes have validated their flexibility under mild conditions with $\varepsilon N$ values below 1000. Our study showed that the patterned EGaIn electrode fabricated with SSWT under harsher conditions with an $\varepsilon N$ value of 1250 exhibited comparable or superior flexibility when compared to previously reported flexible electrodes made of materials such as metal nanowires, metal nanomeshes, graphene, carbon nanotube (CNT), indium tin oxide (ITO), ITO/Ag/ITO (IAI), and poly(3,4-ethylenedioxythiophene):poly(styrenesulfonate) (PEDOT:PSS) films [25,29–40].

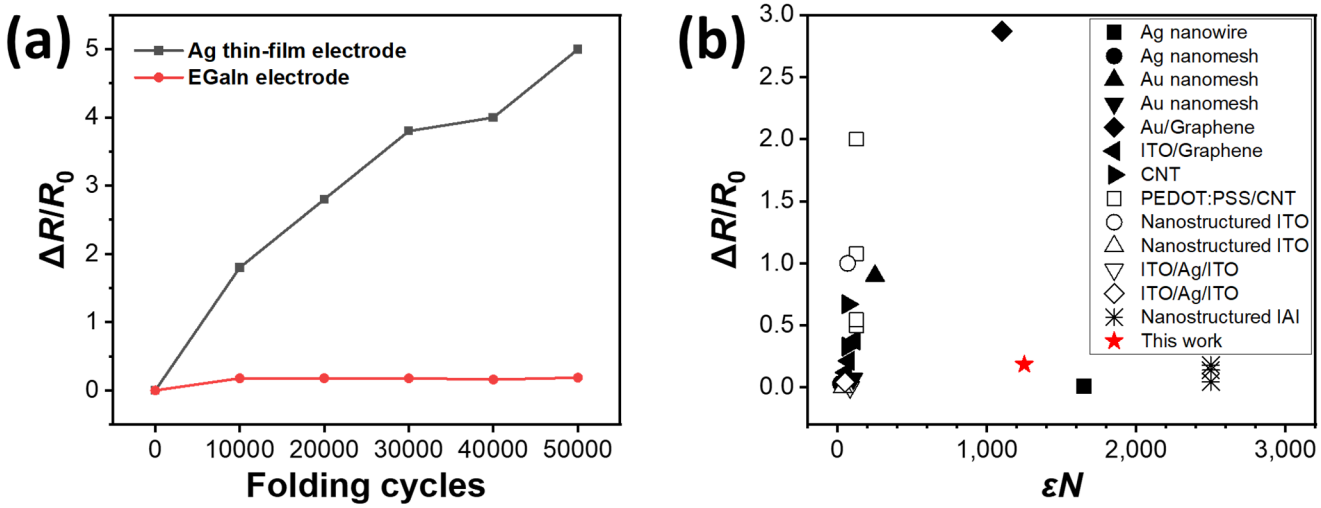


**Figure 6.** Inward-folding cyclic fatigue-deformation characteristics of electrodes: (**a**) change in resistance behaviors of patterned EGaIn liquid metal and Ag thin film electrodes under cyclic folding condition ($\varepsilon$ = 2.5%, $N$ = 50,000, $\varepsilon N$ = 1250) and (**b**) change in resistance with respect to degree of cyclic folding fatigue of patterned EGaIn electrode fabricated with SSWT compared to those of previously reported flexible electrodes: Ag nanowire [29], Ag nanomesh [30], Au nanomesh [31,32], Au/Graphene [33], ITO/Graphene [34], CNT [35], PEDOT:PSS/CNT [36], Nanostructured ITO [37,38], ITO/Ag/ITO [39,40], Nanostructured IAI [25].

## 4. Conclusions

In this work, we presented a simple method to easily fabricate flexible finely and directly patterned EGaIn electrodes using SSWT based on $\gamma_s$ differences. All fabrication steps utilized a solution process that can be carried out under atmospheric conditions, and direct patterning was made possible by UV pulsed laser ablation, which is inexpensive and applicable to large areas. We also investigated the mechanism by which UV-pulsed laser ablation effectively removed the SAM-treated ZnO nanorod array, rendering the liquid metal superhydrophobic, and induced an increase in $\gamma_s$, resulting in improved liquid metal wettability and patterning, using surface analysis. The linewidths of the EGaIn liquid metal patterns fabricated with SSWT could be freely adjusted to realize linewidths as fine as 50 μm. The EGaIn liquid metal patterned electrode fabricated on a flexible substrate exhibited significantly better flexibility than the Ag thin film electrode under severe conditions with an $\varepsilon N$ value of 1250, corresponding to 50,000 cycles of folding fatigue at a peak strain of 2.5%. The simple and easily implementable liquid metal patterning technique proposed in this study, when combined with a passivation layer to protect the liquid metal electrodes, may potentially be applied in the promising field of wearable and stretchable electronics, which requires extreme flexibility.

**Author Contributions:** Conceptualization, C.Y.; data curation, S.J.P.; formal analysis, S.J.P.; funding acquisition, C.Y.; methodology, C.Y.; investigation, C.Y.; project administration, C.Y.; resources, C.Y.; supervision, C.Y.; validation, S.J.P. and C.Y.; visualization, S.J.P. and C.Y.; writing—original draft preparation, S.J.P. and C.Y.; writing—review and editing, C.Y. All authors have read and agreed to the published version of the manuscript.

**Funding:** This work was supported by Enterprise Demand-based Production Technology Commercialization Project of the Korea Institute of Industrial Technology (KITECH), and granted financial resources from the Ministry of Economy and Finance, Republic of Korea (No. JD230008).

**Institutional Review Board Statement:** Not applicable.

**Informed Consent Statement:** Not applicable.

**Data Availability Statement:** Data are contained within the article.

**Conflicts of Interest:** The authors declare no conflict of interest.

## References

1. Chen, G.; Wang, H.; Guo, R.; Duan, M.; Zhang, Y.; Liu, J. Superelastic EGaIn composite fibers sustaining 500% tensile strain with superior electrical conductivity for wearable electronics. *ACS Appl. Mater. Interfaces* **2020**, *12*, 6112–6118. [CrossRef] [PubMed]
2. Li, S.; Chen, X.; Li, X.; Tian, H.; Wang, C.; Nie, B.; He, J.; Shao, J. Bioinspired robot skin with mechanically gated electron channels for sliding tactile perception. *Sci. Adv.* **2022**, *8*, eade0720. [CrossRef] [PubMed]
3. Kim, B.-J.; Shin, H.-A.S.; Jung, S.-Y.; Cho, Y.; Kraft, O.; Choi, I.-S.; Joo, Y.-C. Crack nucleation during mechanical fatigue in thin metal films on flexible substrates. *Acta Mater.* **2013**, *61*, 3473–3481. [CrossRef]
4. Bo, G.; Ren, L.; Xu, X.; Du, Y.; Dou, S. Recent progress on liquid metals and their applications. *Adv. Phys. X* **2018**, *3*, 1446359. [CrossRef]
5. Clarkson, T.W.; Magos, L. The toxicology of mercury and its chemical compounds. *Crit. Rev. Toxicol.* **2006**, *36*, 609–662. [CrossRef] [PubMed]
6. French, S.J.; Saunders, D.J.; Ingle, G.W. The system gallium-indium. *J. Phys. Chem.* **2002**, *42*, 265–274. [CrossRef]
7. Chen, X.; Sun, P.; Tian, H.; Li, X.; Wang, C.; Duan, J.; Luo, Y.; Li, S.; Chen, X.; Shao, J. Self-healing and stretchable conductor based on embedded liquid metal patterns within imprintable dynamic covalent elastomer. *J. Mater. Chem. C* **2022**, *10*, 1039–1047. [CrossRef]
8. Hao, X.P.; Li, C.Y.; Zhang, C.W.; Du, M.; Ying, Z.; Zheng, Q.; Wu, Z.L. Self-shaping soft electronics based on patterned hydrogel with stencil-printed liquid metal. *Adv. Funct. Mater.* **2021**, *31*, 2105481. [CrossRef]
9. Yan, J.; Lu, Y.; Chen, G.; Yang, M.; Gu, Z. Advances in liquid metals for biomedical applications. *Chem. Soc. Rev.* **2018**, *47*, 2518–2533. [CrossRef]
10. Boley, J.W.; White, E.L.; Chiu, G.T.C.; Kramer, R.K. Direct writing of gallium-indium alloy for stretchable electronics. *Adv. Funct. Mater.* **2014**, *24*, 3501–3507. [CrossRef]

11. Park, C.W.; Moon, Y.G.; Seong, H.; Jung, S.W.; Oh, J.-Y.; Na, B.S.; Park, N.-M.; Lee, S.S.; Im, S.G.; Koo, J.B. Photolithography-based patterning of liquid metal interconnects for monolithically integrated stretchable circuits. *ACS Appl. Mater. Interfaces* **2016**, *8*, 15459–15465. [CrossRef] [PubMed]
12. Yang, J.; Zhou, T.; Zhang, L.; Zhu, D.; Handschuh-Wang, S.; Liu, Z.; Kong, T.; Liu, Y.; Zhang, J.; Zhou, X. Defect-free, high resolution patterning of liquid metals using reversibly sealed, reusable polydimethylsiloxane microchannels for flexible electronic applications. *J. Mater. Chem. C* **2017**, *5*, 6790–6797. [CrossRef]
13. Zhang, S.; Wang, B.; Jiang, J.; Wu, K.; Guo, C.F.; Wu, Z. High-fidelity conformal printing of 3D liquid alloy circuits for soft electronics. *ACS Appl. Mater. Interfaces* **2019**, *11*, 7148–7156. [CrossRef] [PubMed]
14. Jiang, Y.; Su, S.; Peng, H.; Kwok, H.S.; Zhou, X.; Chen, S. Selective wetting/dewetting for controllable patterning of liquid metal electrodes for all-printed device application. *J. Mater. Chem. C* **2017**, *5*, 12378–12383. [CrossRef]
15. Yang, C.; Hong, K.; Jang, J.; Chung, D.S.; An, T.K.; Choi, W.S.; Park, C.E. Solution-processed flexible ZnO transparent thin-film transistors with a polymer gate dielectric fabricated by microwave heating. *Nanotechnology* **2009**, *20*, 465201. [CrossRef] [PubMed]
16. Yang, C.; Kwack, Y.; Kim, S.H.; An, T.K.; Hong, K.; Nam, S.; Park, M.; Choi, W.-S.; Park, C.E. Ambipolar thin-film transistors and an inverter based on pentacene/self-assembled monolayer modified ZnO hybrid structures for balanced hole and electron mobilities. *Org. Electron.* **2011**, *12*, 411–418. [CrossRef]
17. Çolak, H.; Karaköse, E.; Kartopu, G. Effect of consumption of the sol–gel deposited ZnO seed layer on the growth and properties of high quality ZnO nanorods. *J. Mater. Sci. Mater. Electron.* **2018**, *29*, 11964–11971. [CrossRef]
18. Usha, A.; Christy, J. Characterization, thermal effect on optical band gap energy and photoluminescence in wurtzite ZnO: Er nanocrystallites. *Mater. Today Proc.* **2016**, *3*, 145–151. [CrossRef]
19. Ravi-Kumar, S.; Lies, B.; Zhang, X.; Lyu, H.; Qin, H. Laser ablation of polymers: A review. *Polym. Int.* **2019**, *68*, 1391–1401. [CrossRef]
20. Lee, H.-L.; Hussain, A.; Moon, Y.-J.; Hwang, J.Y.; Moon, S.J. Influence of pre-sintering on the nanosecond pulsed laser ablation patterns of spin-coated silver nanoparticles. *Appl. Phys. A* **2023**, *129*, 705. [CrossRef]
21. Lee, J.; Yong, K. Combining the lotus leaf effect with artificial photosynthesis: Regeneration of underwater superhydrophobicity of hierarchical ZnO/Si surfaces by solar water splitting. *NPG Asia Mater.* **2015**, *7*, e201. [CrossRef]
22. Kinloch, A.J. *Adhesion and Adhesives: Science and Technology*; Springer: Berlin, Germany, 1987; ISBN 978-0-412-27440-4.
23. Sim, I.; Park, S.; Shin, K.Y.; Yang, C.; Kang, H.; Hwang, J.Y.; Moon, S.J. Inkjet printing of high aspect ratio silver lines via laser-induced selective surface wetting technique. *Coatings* **2023**, *13*, 683. [CrossRef]
24. Mao, L.; Meng, Q.; Ahmad, A.; Wei, Z. Mechanical analyses and structural design requirements for flexible energy storage devices. *Adv. Energy Mater.* **2017**, *7*, 1700535. [CrossRef]
25. Han, S.; Ju, B.K.; Yang, C. Ultra-flexible and transparent electrodes with controllable crack length via metal–polymer hybrid nanostructure. *Thin Solid Film.* **2022**, *757*, 139388. [CrossRef]
26. Zhao, Z.; Soni, S.; Lee, T.; Nijhuis, C.A.; Xiang, D. Smart eutectic gallium–indium: From properties to applications. *Adv. Mater.* **2023**, *35*, 2203391. [CrossRef] [PubMed]
27. Park, Y.-G.; Lee, G.-Y.; Jang, J.; Yun, S.M.; Kim, E.; Park, J.-U. Liquid metal-based soft electronics for wearable healthcare. *Adv. Healthc. Mater.* **2021**, *10*, 2002280. [CrossRef] [PubMed]
28. Chen, S.; Wang, H.-Z.; Zhao, R.-Q.; Rao, W.; Liu, J. Liquid metal composites. *Matter* **2020**, *2*, 1446. [CrossRef]
29. Kim, S.; Lee, H.; Kim, D.; Ha, H.; Qaiser, N.; Yi, H.; Hwang, B. Ethylcellulose/Ag nanowire composites as multifunctional patchable transparent electrodes. *Surf. Coat. Technol.* **2020**, *394*, 125898. [CrossRef]
30. Song, M.; Kim, H.-J.; Kim, C.S.; Jeong, J.-H.; Cho, C.; Lee, J.-Y.; Jin, S.-H.; Choi, D.-G.; Kim, D.-H. ITO-free highly bendable and efficient organic solar cells with Ag nanomesh/ZnO hybrid electrodes. *J. Mater. Chem. A* **2015**, *3*, 65–70. [CrossRef]
31. Guo, C.F.; Sun, T.; Liu, Q.; Suo, Z.; Ren, Z. Highly stretchable and transparent nanomesh electrodes made by grain boundary lithography. *Nat. Commun.* **2014**, *5*, 3121. [CrossRef]
32. Chauvin, A.; Txia Cha Heu, W.; Buh, J.; Tessier, P.-Y.; El Mel, A.-A. Vapor dealloying of ultra-thin films: A promising concept for the fabrication of highly flexible transparent conductive metal nanomesh electrodes. *NPJ Flex. Electron.* **2019**, *3*, 5. [CrossRef]
33. Cho, C.; Kang, P.; Taqieddin, A.; Jing, Y.; Yong, K.; Kim, J.M.; Haque, M.F.; Aluru, N.R.; Nam, S.W. Strain-resilient electrical functionality in thin-film metal electrodes using two-dimensional interlayers. *Nat. Electron.* **2021**, *4*, 126–133. [CrossRef]
34. Lee, S.J.; Kim, Y.; Hwang, J.-Y.; Lee, J.-H.; Jung, S.; Park, H.; Cho, S.; Nahm, S.; Yang, W.S.; Kim, H.; et al. Flexible indium-tin oxide crystal on plastic substrates supported by graphene monolayer. *Sci. Rep.* **2017**, *7*, 3131. [CrossRef] [PubMed]
35. Han, S.-H.; Kim, B.-J.; Park, J.-S. Surface modification of plastic substrates via corona-pretreatment and its effects on the properties of carbon nanotubes for use of flexible transparent electrodes. *Surf. Coat. Technol.* **2015**, *271*, 100–105. [CrossRef]
36. Kim, B.-J.; Han, S.-H.; Park, J.-S. Properties of CNTs coated by PEDOT:PSS films via spin-coating and electrophoretic deposition methods for flexible transparent electrodes. *Surf. Coat. Technol.* **2015**, *271*, 22–26. [CrossRef]
37. Königer, T.; Münstedt, H. Coatings of indium tin oxide nanoparticles on various flexible polymer substrates: Influence of surface topography and oscillatory bending on electrical properties. *J. Soc. Inf. Disp.* **2008**, *16*, 559–568. [CrossRef]
38. Yun, J.; Park, Y.H.; Bae, T.-S.; Lee, S.; Lee, G.-H. Fabrication of a completely transparent and highly flexible ITO nanoparticle electrode at room temperature. *ACS Appl. Mater. Interfaces* **2013**, *5*, 164–172. [CrossRef] [PubMed]

39. Kim, T.-H.; Park, S.-H.; Kim, D.-H.; Nah, Y.-C.; Kim, H.-K. Roll-to-roll sputtered ITO/Ag/ITO multilayers for highly transparent and flexible electrochromic applications. *Sol. Energy Mater. Sol. Cells* **2017**, *160*, 203–210. [CrossRef]
40. Wu, C.-C. Highly flexible touch screen panel fabricated with silver-inserted transparent ITO triple-layer structures. *RSC Adv.* **2018**, *8*, 11862–11870. [CrossRef]

**Disclaimer/Publisher's Note:** The statements, opinions and data contained in all publications are solely those of the individual author(s) and contributor(s) and not of MDPI and/or the editor(s). MDPI and/or the editor(s) disclaim responsibility for any injury to people or property resulting from any ideas, methods, instructions or products referred to in the content.